

Magnetic chemically peculiar stars investigated by the Solar Mass Ejection Imager

E. Paunzen,¹★ J. Supíková,^{1,2} K. Bernhard,^{3,4} S. Hümmerich,^{3,4} M. Prišegen¹

¹*Department of Theoretical Physics and Astrophysics, Masaryk University, Kotlářská 2, CZ611 37 Brno, Czech Republic*

²*Faculty of Informatics, Masaryk University, Brno, Czech Republic*

³*Bundesdeutsche Arbeitsgemeinschaft für Veränderliche Sterne e.V. (BAV), Berlin, Germany*

⁴*American Association of Variable Star Observers (AAVSO), Cambridge, USA*

Accepted XXX. Received YYY; in original form ZZZ

ABSTRACT

Since the discovery of the spectral peculiarities of their prototype α^2 Canum Venaticorum in 1897, the so-called ACV variables, which are comprised of several groups of chemically peculiar stars of the upper main sequence, have been the target of numerous photometric and spectroscopic studies. Especially for the brighter ACV variables, continuous observations over about a century are available, which are important to study long-term effects such as period changes or magnetic cycles in these objects. The present work presents an analysis of 165 Ap/CP2 and He-weak/CP4 stars using light curves obtained by the Solar Mass Ejection Imager (SMEI) between the years 2003 and 2011. These data fill an important gap in observations for bright ACV variables between the *Hipparcos* and TESS satellite missions. Using specifically tailored data treatment and period search approaches, we find variability in the accuracy limit of the employed data in 84 objects. The derived periods are in excellent agreement with the literature; for one star, the here presented solution represents the first published period. We discuss the apparently constant stars and the corresponding level of non-variability. From an investigation of our target star sample in the Hertzsprung-Russell diagram, we deduce ages between 100 Myr and 1 Gyr for the majority of our sample stars. Our results support that the variable CP2/4 stars are in a more advanced evolutionary state and that He and Si peculiarities, preferentially found in the hotter, and thus more massive, CP stars, produce larger spots or spots of higher contrast.

Key words: stars: chemically peculiar - early-type - variables: General - Hertzsprung-Russell and colour–magnitude diagrams

1 INTRODUCTION

Chemically peculiar (CP) stars form a significant fraction (up to 15%) of upper main-sequence stars and are mostly found between spectral types early B to early F. The defining characteristic of CP stars is the presence of spectral peculiarities, which indicate unusual elemental abundance patterns. Several groups of CP stars have been defined, such as the metallic-line or Am (CP1) stars, the magnetic Bp/Ap (CP2) stars, the Mercury-Manganese (HgMn/CP3) stars, and the He-weak (CP4) stars (Preston 1974; Ghazaryan et al. 2018, 2019).

The CP2 and CP4 stars are distinguished from the CP1 and CP3 stars by the presence of globally organized magnetic fields with strengths of about 300 G to several tens of kiloGauss (Romanyuk & Kudryavtsev 2008). Stibbs (1950) introduced the Oblique Rotator model of magnetic stars, which assumes non-coincidence of

magnetic and rotational axes and is able to reproduce the observed variability and the reversals of the magnetic field strength. Due to chemical abundance concentrations at the magnetic poles, CP2/4 stars also show spectral and photometric variability, as well as radial velocity variations of the appearing and receding patches on the stellar surface, which are also easily understood in terms of the Oblique Rotator model. Variable CP2/4 stars are traditionally referred to as α^2 Canum Venaticorum (ACV) variables (Samus' et al. 2017) and are characterised by light curves that remain stable over decades or more.

There is a long tradition of photographic and photoelectric investigations of bright ACV variables in the literature (Abt & Golson 1962; Peterson 1970; Hensberge et al. 1981; Adelman & Pypers 1993a; Dukes & Adelman 2018). The present work concentrates on the analysis of bona-fide CP2 and CP4 stars using light curves from the Solar Mass Ejection Imager (SMEI, Eyles et al. 2003), which continuously observed bright stars ($V < 7$ mag) from 2003 to 2011.

For the analysis of the long-term behaviour of chemical spots

★ E-mail: epaunzen@physics.muni.cz

on the surface of CP2/4 stars, it is essential to have photometric observations with a long time baseline. Effects such as magnetic cycles and long-term variations of the rotational period are rarely investigated, and no data are currently available for a statistically sound sample of these stars. For example, precise observations with long time baselines are needed for the analysis of rotational period changes in ACV variables, and only very few of these stars are currently known which underwent measurable changes (Mikulášek 2016).

If an analysis of the long-term behaviour of ACV variables is to include data from photographic plates, such as the data provided the Digital Access to a Sky Century@Harvard (DASCH) project (Tang et al. 2013), we are mainly limited to bright stars. For these objects, many photoelectric studies, beginning in the 1950s, are available. However, since the beginning of CCD photometry, observations of bright stars have become scarce in the literature.

Before this background, the photometric observations of the SMEI satellite fill an important gap in time between the *Hipparcos* mission (Eyer et al. 1994) and the observations of the Transiting Exoplanet Survey Satellite (TESS, Ricker et al. 2015), which started in April 2018 and is observing stars as bright as 4th magnitude. The bright objects targeted by these missions have not been observed by the All Sky Automated Survey (ASAS-3, Pojmanski 2002), the Wide Angle Search for Planets (WASP, Pollacco et al. 2006), and similar surveys because of saturation issues.

In general, TESS data are superior in precision to the SMEI data. However, for about 25 % of our sample stars, no TESS photometry is available yet. Furthermore, the time baseline of the TESS data is still short and, in many cases, covers only some rotational cycles. The time baseline of the SMEI data, on the other hand, is much longer and therefore better suited to derive rotational periods with a precision sufficient to our goals. In addition to that, several bright stars show saturation issues in TESS data, which are not observed in the SMEI data sets. The analysis of SMEI data, therefore, is important for the study of bright ACV variables, for which ground-based follow-up spectroscopic and spectropolarimetric observations are comparatively easy to achieve.

In total, we analysed the light curves of 165 stars, 84 of which show variability in the accuracy limits of the SMEI data. Except for one star, all variables have literature periods, so the data can be employed for the study of their long-term behaviour. We furthermore discuss the noise limits of the amplitude spectra of the non-variable CP2/4 stars. We emphasise that the recent papers discussing the characteristics of ACV variables (Bernhard et al. 2015; Hümmelich et al. 2016; Bernhard et al. 2020) do not derive any statistics on non-variable CP2/4 stars which should also have spots on their surfaces and thus should show variability. The boundary conditions of when ACV variability occurs are, in general, poorly studied.

In addition, we discuss the location of our target star sample within the classical Hertzsprung-Russell diagram and compare the available parallaxes and luminosities of the *Hipparcos* and *Gaia* missions.

2 DATA SOURCES AND TARGET SELECTION

We searched for all probable CP2 and CP4 stars in the most up-to-date collection, the most recent version of the General Catalogue of CP Stars published by Renson & Manfroid (2009). Because SMEI observed only bright, and hence for the most part well studied, stars (Fig. 1), the classifications in this catalogue should be reliable. However, we also included some borderline cases for which the spectral

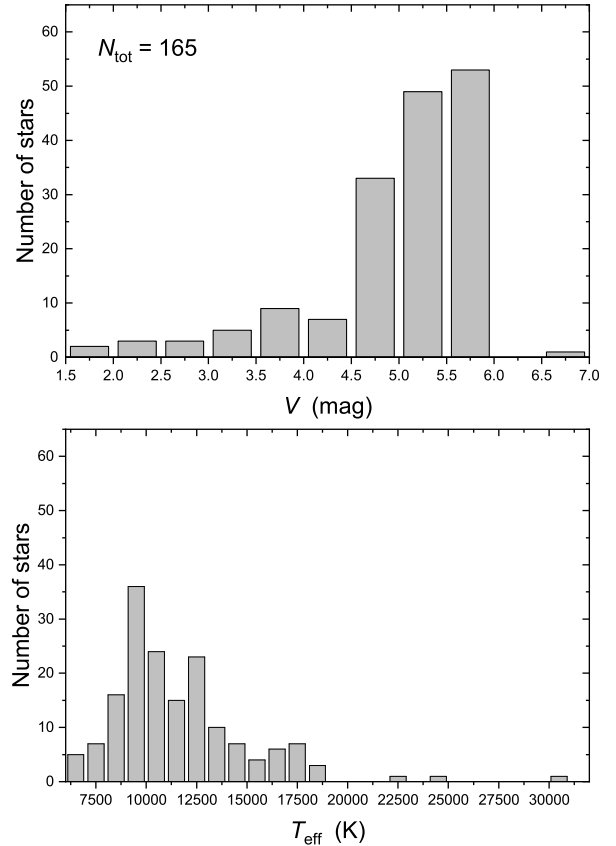


Figure 1. Histograms of the V magnitudes (upper panel) and effective temperatures (lower panel) of our target star sample.

classification is not clear. Here we recall the remarks of Renson & Manfroid (2009) on the classification of CP stars: "I" – a star improperly considered Ap or Am; "?" – CP star of doubtful nature; and "*" – well-known Ap or Am star. Although these classifications have to be viewed with caution, we excluded all stars denoted with a "?". In total, 165 stars were selected as our final sample. Essential data for these objects are given in Table A1.

The Solar Mass Ejection Imager (SMEI, Eyles et al. 2003) was launched into an Earth-terminator, Sun-synchronous, 840 km polar orbit as a secondary payload on board the Coriolis spacecraft in January 2003 and was terminated in September 2011. Its main purpose was to monitor and predict space weather in the inner solar system.

SMEI comprised three wide-field cameras, which were aligned such that the total field of view is a 180 deg and about 3 deg wide arc, yielding a near-complete image of the sky after about every 101.5 min orbit. The photometric passband ranges from 450 to 950 nm. Several papers (for example, Walczak et al. 2019; Zwintz et al. 2019) successfully employed the long time-baseline SMEI photometry for the study of variable stars.

A detailed description of the data analysis pipeline used to

extract light curves from the raw data is provided by Hick et al. (2007). Stellar time series can be extracted from the SMEI website¹.

3 TIME SERIES ANALYSIS

The time series analysis described in this section was performed with the program packages PERANSO (Paunzen & Vanmunster 2016) and VARTOOLS (Hartman & Bakos 2016). For the identification of significant periods, the Generalized Lomb-Scargle algorithm (L-S, Zechmeister & Kürster 2009) and the Phase-Dispersion Method (PDM, Stellingwerf 1978) were applied. Both methods complement each other well, especially in the case of the SMEI data sets which are not free of various instrumental effects (Sect. 3.1).

The PDM algorithm is a classical string-length method. First of all, the data are folded on a series of trial periods. For each of these, the original data are assigned phases which are then re-ordered in ascending sequence. The reordered data are examined by inspection across the full phase interval between zero and one. For each trial period, the full phase interval is divided into a number of bins. Then, the sum of the lengths of line segments joining successive points (the string-length) is calculated. The variance of each of these bins is derived, giving a measure of the scatter around the mean light curve, defined by the means of the data in each sample. The PDM statistic is then calculated by dividing the overall variance of all the samples by the variance of the original (unbinned) data set. This process is repeated for each consecutive trial period. Minima in the plot of the string-length versus the trial period can be considered as corresponding to the underlying period.

The L-S algorithm is a variation of the Discrete Fourier Transform (DFT) which converts a finite list of equally spaced samples of a function (here the light curve) into a list of coefficients of a linear combination of sinusoidal and cosinusoidal functions. The data are transformed from the time to the frequency domain (Lomb-Scargle periodogram), invariant to time shifts. From a statistical point of view, the resulting periodogram is related to the χ^2 for a least-squares fit of a single sinusoid to the data which can treat heteroscedastic measurement uncertainties. The underlying model is non-linear in frequency and the basis functions at different frequencies are not orthogonal.

For interpreting the significance of the detected periods, we used the False-Alarm probability (FAP), which denotes the probability that at least one out of N independent power values in a prescribed search band of a power (or amplitude) spectrum computed from a white-noise time series is expected to be as large as or larger than a given value. Its correct interpretation has been often discussed in the literature (Horne & Baliunas 1986; Cumming et al. 1999). Here, we consider a period significant if the log FAP value is larger than 1000. Furthermore, we require that this period is unambiguously detected with both the L-S and PDM methods. These are very strict limits that we feel justified to apply due to the characteristics of the SMEI light curves.

3.1 Instrumental effects and data cleaning

SMEI light curves are strongly influenced by the Sun, Moon and daily cycles. The period range of ACV variables spans several magnitudes, extending from about half a day (Hümmerich et al. 2017) to

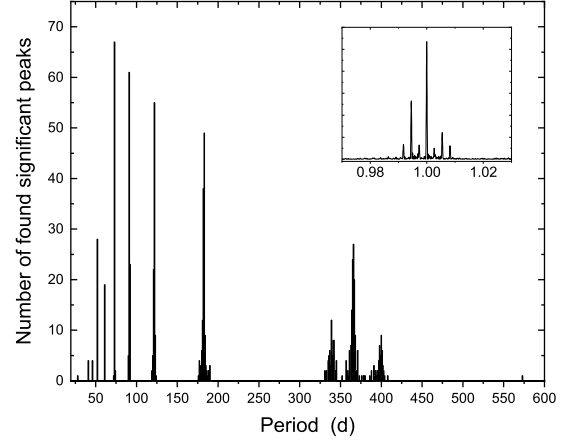


Figure 2. Histogram of detected instrumental periods in the range from 20 to 1000 days. Only periods detected more than two times are shown (there are none in the range from 600 to 1000 days). The panel in the right upper corner shows a typical L-S periodogram around the period of one day.

hundreds or even thousands of years (Mathys 2017). However, most ACV variables show periods of days (Netopil et al. 2017). Because of this, the SMEI orbital period of 101.5 min, which introduces artificial signals in the high frequency range, should not influence our results significantly.

To further investigate this matter, all 165 light curves were searched to identify the most important instrumentally-induced periods. The L-S algorithm was used to search for signals in the range from 20 to 1000 days, and the data were consecutively pre-whitened with the most significant periods, after which the L-S algorithm was applied again. This procedure was carried out five times.

In Fig. 2, we present the histogram (binned to one day intervals) of the derived instrumental periods. Only periods detected more than two times are shown; none were found in the range from 600 to 1000 days. In 111 out of the 165 light curves, the period around one year is the most significant one, followed by the half year period for an additional 47 light curves. Overall, we found significant peaks at around 52, 61, 73, 91, 122, 183, and 366 days. We also note the strong "side lobes" of the one year period around 339 and 400 days. In addition, a one day period with a typical pattern is clearly visible in the periodograms (Fig. 2, upper right corner).

All cleaning and time series analysis steps are demonstrated using the light curve of HD 128898 (α Cir), which is a rapidly oscillating Ap (roAp) star that also shows low-amplitude ACV variations (Bruntt et al. 2009). Together with photometric data from the BRITE Constellation, TESS, and WIRE satellites, its SMEI light curve was used in the recent paper of Weiss et al. (2020) to study the spot structure of the star. Unfortunately, in their paper, the authors do not show amplitude spectra based on SMEI data (see Figs. 5 and 6 therein). The following automatic procedure was applied to all light curves.

- Step 1: cleaning of the raw light curve using a basic σ -clipping algorithm
- Step 2: consecutive prewhitening of the five periods with the

¹ <http://smei.ucsd.edu/>

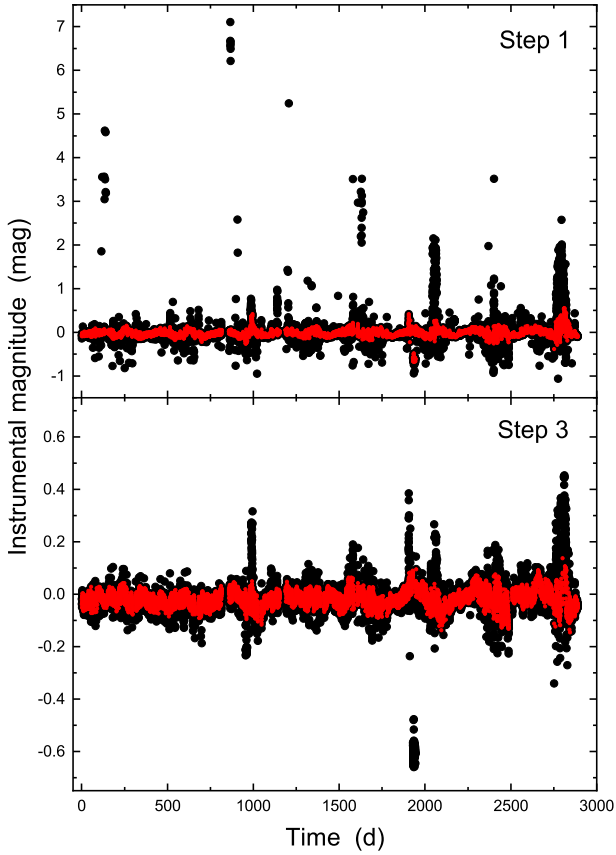


Figure 3. Example of the reduction steps one and three as described in Section 3.1. The light curve is that of the star HD 128898 (α Cir). Red dots denote magnitudes after the application of the corresponding reduction step.

highest FAP in the range from 50 to 1000 days and the one day period

- Step 3: cleaning of the residual light curve using a basic σ -clipping algorithm
- Step 4: search for significant periods

Fig. 3 illustrates the first and third steps graphically. It also highlights the strong instrumental trends present in the raw light curve.

3.2 Variable stars

In total, we identified 84 variable stars, from which 83 have periods in the International Variable Star Index (VSX, Watson et al. 2006) of the American Association of Variable Star Observers and the compilations of Netopil et al. (2017) and Jagelka et al. (2019). Example phased light curves of three sample stars (HD 11502, HD 25823, and HD 74067) are shown in Figure 4. The different light curves characteristics relating to the spot distribution on the surfaces are nicely visible.

In Fig. 5, we present a comparison of the here derived periods to the literature periods of the stars listed in Table 1. The typical period error amounts to 0.0001 d. Because in orientations where two spots come into view during a star’s rotation cycle, a significant

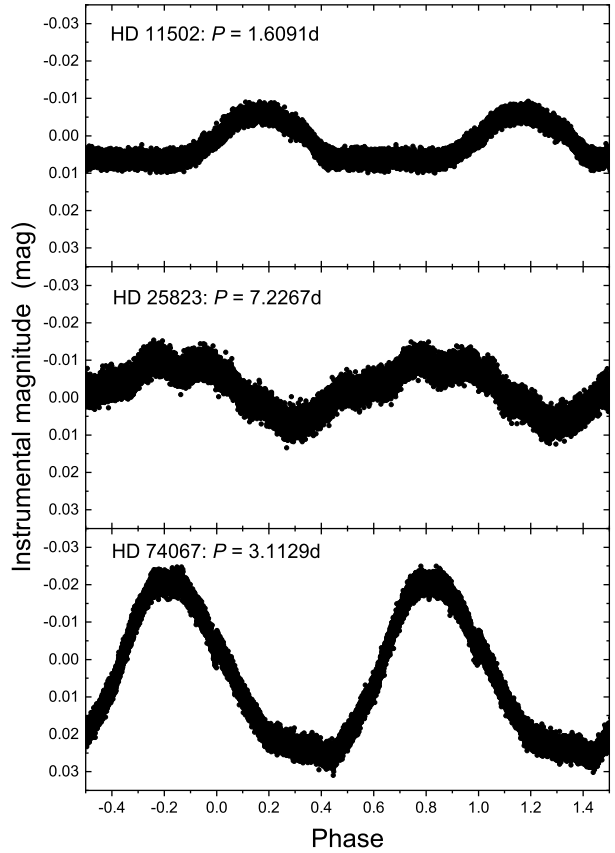


Figure 4. Phased SMEI light curves of three sample stars with widely different periods and light curve characteristics.

number of ACV variables exhibit double-waved light curves (Hümmerich et al. 2016). Therefore, a twice longer (or shorter) rotation period is sometimes possible, in particular for objects with very small amplitudes and/or significant scatter in their light curves. We emphasise that the given period values correspond to the periods with the highest FAP values; nevertheless, the most prominent periods may sometimes represent harmonics of the true rotation period, as becomes obvious from Fig. 5. In ambiguous cases, the true period has to be determined by other means such as radial velocity studies.

One object (HD 82984) is listed as “CST:” in the VSX, that is, as a non-variable (constant) star, which was formerly suspected to be a variable. This classification goes back to Jerzykiewicz & Sterken (1977), who did not discuss HD 82984 in more detail. No further references to a photometric time-series study of this object were found in the literature; we are therefore confident that the here presented solution is the first published period of this star.

There are three obvious outliers in Fig. 5, which are discussed in more detail below.

HD 183056: Williams et al. (1974) reported variability of the H β -line profile on the basis of 49 scans taken during a time span of 188 min. Later on, Winzer (1974) reported a possible period of 0.68674 d for this star, whereas Adelman & Pyper (1993b) concluded that if variability is present, the amplitude has to be below

Table 1. Significant periods of the 84 stars of our target star sample that show variability in the accuracy limit of the SMEI data, as based on the time-series analysis described in Section 3. Literature periods were gleaned from the International Variable Star Index (VSX, [Watson et al. 2006](#)) and the compilations of [Netopil et al. \(2017\)](#) and [Jagelka et al. \(2019\)](#). The typical period error amounts to 0.0001 d.

HD	P_{SMEI} (d)	P_{Lit} (d)	HD	P_{SMEI} (d)	P_{Lit} (d)	HD	P_{SMEI} (d)	P_{Lit} (d)	HD	P_{SMEI} (d)	P_{Lit} (d)
3980	1.9758	3.9516	36485	2.8662	5.7325	96616	2.4292	2.4330	148112	3.0437	2.9510
10221	3.1538	3.1848	39317	2.6571	2.6569	103192	2.3567	2.3440	148898	2.9642	2.9900
11502	1.6091	1.6092	40312	3.6186	3.6187	108662	5.0761	5.0633	150549	3.7597	3.7600
12767	1.8923	1.8923	40394	14.3661	14.3680	109026	2.7280	2.7293	151525	4.1163	4.1160
14392	1.3086	1.3080	47144	2.2105	2.2100	112185	5.0889	5.0886	152107	3.8575	3.8567
15089	1.7403	1.7405	47152	2.7112	2.7112	118022	3.7225	3.7220	152564	2.1635	2.1637
18296	1.4421	2.8842	54118	3.2752	3.2753	120198	1.3858	1.3800	166596	1.6299	1.6700
19832	0.7279	0.7279	56022	0.9184	0.9183	124224	0.5207	0.5207	168733	6.3526	6.3000
21699	2.4920	2.4761	56455	2.0583	2.0580	125823	8.8166	8.8171	170000	1.7166	1.7165
22470	1.9289	1.9300	59256	0.9812	0.9430	128898	8.9051	0.0047	175362	3.6741	3.6740
22920	3.9471	3.9474	66624	1.9983	1.9984	130158	4.4142	4.4136	182255	1.2622	1.2600
23408	20.3234	10.2880	72968	5.6520	11.3050	131120	1.5687	1.5690	183056	0.7450	0.6870
25267	1.2099	1.2094	73340	2.6676	2.6675	133880	0.8775	0.8775	183806	3.1197	2.9210
25823	7.2267	7.2274	74067	3.1129	3.1130	134759	1.5566	3.0993	196178	1.0041	1.0060
26961	1.5274	1.5274	74521	7.0519	6.9071	137909	18.2751	18.4870	196502	10.1376	20.2750
27309	1.5689	1.5690	74560	1.5509	1.5511	138764	1.2586	1.2588	201433	1.1260	1.4289
28843	1.3738	1.3740	77653	1.4878	1.4878	138769	2.0895	2.0894	201834	3.5351	3.5354
29009	3.8002	3.8200	79158	1.9174	3.8340	140160	1.5958	1.5958	209515	2.3870	2.3880
29305	2.9432	2.9500	82984	6.0878		140728	1.2956	1.3049	220825	1.4149	1.4150
32549	4.6396	4.6397	92664	1.6731	1.6680	142096	6.6411	3.3136	221006	2.3148	2.3148
32650	2.7350	2.7348	93030	2.2031	2.2027	142990	0.9789	0.9789	223640	3.7350	3.7352

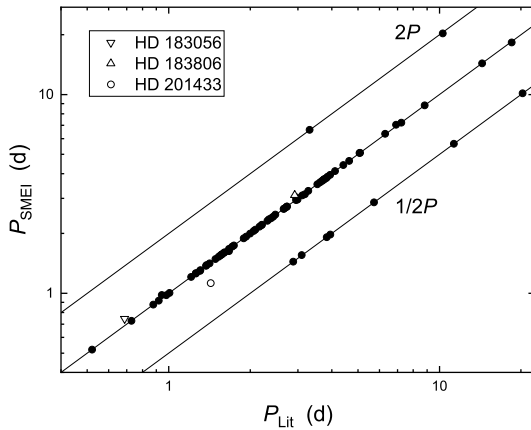


Figure 5. Comparison of the period values derived from SMEI data to the literature periods for our sample stars. Also indicated are the unity line and the lines corresponding to the half- and double-periods. Open symbols denote the three outliers (HD 183056, HD 183806, and HD 201433), which are discussed in the text.

0.02 mag. HD 183056 was included in the *Hipparcos*-based study of [Adelman \(1998\)](#); however, no period solution was presented.

HD 183806: [Mathys & Manfroid \(1985\)](#) measured this star in Strömgren *uvby* filters and reported a possible period of 2.9213 d. No other period information on this star seems to have been pub-

lished. The here derived SMEI period of 3.1197 d is slightly longer than the published one.

HD 201433: This is a single-lined spectroscopic triple system consisting of a massive Slowly Pulsating B (SPB) star orbited by two low-mass stars with periods of about 3.31 and 154 d, respectively ([Kallinger et al. 2017](#)). The amplitude spectrum of the SMEI data is clearly indicative of multiperodicity due to pulsations. The here detected periods (not all listed in Table 1) are compatible with those listed in Table 4 of [Kallinger et al. \(2017\)](#).

All other stars lie well on the correlations presented in Fig. 5, which lends confidence in our time-series analysis.

3.3 Apparently constant stars

Here, we define ‘‘constant’’ as light curves whose amplitude spectra show no significant peaks as defined in Section 3. As first step, we describe the characteristics of the amplitude spectra in more detail.

The noise in the amplitude spectra can be well described as 1/*f* or ‘‘flicker’’ noise. Sometimes it also referred to as ‘‘pink’’ noise ([Subba Rao et al. 1997](#)). It can be described as a linear law by plotting the logarithm of the frequency (*f*) versus the logarithm of the amplitude (*A*).

$$\log A = a + b \log f. \quad (1)$$

The *a* and *b* values of the 81 amplitude spectra without any significant peaks are listed in Table 2. The errors of the parameters *a* and *b* amount to 0.002 and 0.005, respectively, throughout the sample, which implies that the estimates are very robust. The mean slope for the complete sample is $-0.44(5)$, which means that the noise characteristics are not dependent on the individual data sets. The level of the noise characterised by the intercept depends on the number of data points and the magnitude of the stars (photon statistics).

Table 2. Results from fitting the amplitude spectra (Fig. 6) of the apparently constant stars in the form $\log A = a + b \log f$, where A is the amplitude and f the frequency. Throughout the sample, the errors relating to the parameters a and b amount to 0.002 and 0.005, respectively

HD	a	b	HD	a	b	HD	a	b	HD	a	b
1280	-3.944	-0.461	64740	-3.976	-0.414	108945	-3.723	-0.448	181615	-3.722	-0.550
2054	-3.765	-0.445	68351	-3.563	-0.458	115735	-3.901	-0.443	182568	-3.824	-0.454
4853	-3.840	-0.492	68601	-3.990	-0.475	116458	-3.794	-0.335	185872	-3.468	-0.439
5737	-3.837	-0.431	71046	-3.893	-0.317	116656	-4.100	-0.466	187474	-3.634	-0.431
6397	-3.678	-0.471	77350	-3.612	-0.446	120640	-3.454	-0.419	188041	-3.587	-0.380
11753	-3.806	-0.424	78556	-3.526	-0.404	120709	-3.841	-0.490	189178	-3.822	-0.461
18519	-3.950	-0.479	78702	-3.677	-0.370	123255	-3.709	-0.478	196524	-3.990	-0.449
19400	-3.798	-0.331	79416	-3.638	-0.452	124425	-3.755	-0.436	198667	-3.708	-0.407
23850	-3.769	-0.449	81188	-4.092	-0.361	128974	-3.472	-0.464	201601	-3.897	-0.442
28319	-3.858	-0.451	90264	-3.829	-0.370	130109	-3.914	-0.445	202444	-4.050	-0.437
30612	-3.717	-0.333	90972	-3.534	-0.428	135382	-3.918	-0.314	202627	-3.854	-0.461
34968	-3.920	-0.479	92728	-3.666	-0.374	136933	-3.498	-0.449	202671	-3.608	-0.430
35039	-3.925	-0.437	94334	-3.934	-0.417	143699	-3.668	-0.440	203006	-3.758	-0.448
35497	-4.037	-0.463	95418	-4.169	-0.439	148330	-3.917	-0.456	203585	-3.453	-0.450
38104	-3.872	-0.435	96097	-3.675	-0.552	152127	-3.690	-0.414	205637	-3.630	-0.424
42509	-3.413	-0.468	97633	-3.961	-0.487	157740	-3.480	-0.424	206742	-3.916	-0.504
55719	-3.932	-0.444	98664	-3.674	-0.557	169467	-3.813	-0.439	215766	-3.213	-0.407
59635	-3.743	-0.472	101189	-3.607	-0.378	172728	-3.783	-0.476	221760	-3.768	-0.445
61110	-3.828	-0.472	106661	-3.687	-0.510	175156	-3.736	-0.403			
61641	-3.706	-0.429	107696	-3.172	-0.295	177003	-3.779	-0.400			
64486	-3.980	-0.505	108283	-3.723	-0.473	177756	-4.003	-0.470			

In Fig. 6, we present example amplitude spectra of two stars showing, respectively, a low (HD 95418, upper panel) and a high (HD 107696, lower panel) noise level in the investigated frequency domain. The fits are shown as straight lines. In both amplitude spectra, the remains of the one-day frequency are clearly visible.

From the 81 stars without any significant signals in SMEI data, 18 stars have periods in the literature and another 10 stars are flagged as variables or variable star candidates in the VSX. In the following, we discuss these objects in more detail.

In the case of four stars, the literature period exceeds 30 days, which may explain their non-detection in SMEI data: HD 116458 (149.25373 d), HD 181615 (137.9343 d), HD 187474 (2300 d), and HD 188041 (224.5 d).

Wraight et al. (2012) identified low amplitude variations on the basis of STEREO data in HD 6397, HD 68351, and HD 77350.

One of the most valuable sources for the study of bright ACV variables are the data of the *Hipparcos* mission. Adelman (1998) and Paunzen & Maitzen (1998) reported low amplitude variability in HD 73340, HD 79416, HD 201601, HD 202671, HD 203006, HD 205637, and HD 221760.

HD 5737: the amplitude of this He-weak object amounts to only a few mmags in the Strömgren photometric system (Manfroid & Renson 1994).

HD 23850: this star was found constant in light by Wraight et al. (2012).

HD 28319: this is the binary system θ^2 Tauri, the brightest member of the Hyades, which consists of at least two components showing δ Scuti-type pulsations (Armstrong et al. 2006). The existence of rotational variability was never confirmed.

HD 35039: Balona & Engelbrecht (1985) found first evidence for line-profile variations in this star using a limited set of observations. Later on, Le Contel et al. (2001) classified HD 35039 as a SPB star showing multiperiodic radial velocity variations. However, it is a He-rich CP star according to Romanyuk et al. (2013). This

object deserves a new thorough analysis of all spectroscopic data to shed more light on its nature.

HD 68601: this star was found variable by Jerzykiewicz & Sterken (1977), who did not discuss its characteristics in more detail. No other variability study of this object was found in the literature.

HD 107696: this star was part of the long-term photometric survey of variable stars at ESO (Manfroid et al. 1991). However, no detailed results were published on this object by the consortium.

HD 108945: this star was analysed in more detail with photometric and spectroscopic data by Paunzen et al. (2019), who confirmed the existence of rotational light variability but were unable to find any significant frequencies with a semi-amplitude exceeding 0.2 mmag in the high-frequency range.

HD 115735: this is a well-studied ACV variable (Zverko 1984; Zverko et al. 1994).

HD 124425: no time-series analysis was found in the literature.

HD 148330: Ziznovsky (1983) identified radial velocity variations and photometric variability with an amplitude of 17 mmag in the g_2 filter (Paunzen et al. 2005).

HD 215766: this star was found constant by Wraight et al. (2012).

Upper limits of variability were derived for 50 out of 165 objects (~30%) for which no entry about variability exists in the VSX and the literature. The question arises which parameters define the boundary conditions for the occurrence of ACV variability, that is, the presence of spots of sufficient size or contrast on the surface that lead to observable photometric variations.

Jackson & Jeffries (2013) analysed the relationship between size and surface coverage of starspots on magnetically-active low-mass stars. Employing different filling factors, characteristic scale-lengths, and spot distributions in their simulations, they were able to show that small light-curve amplitudes in magnetically active M dwarfs can be explained by a starspot model consisting of large filling factors of dark spots with a random distribution on the stellar surface. To adjust this model to higher mass objects and use it

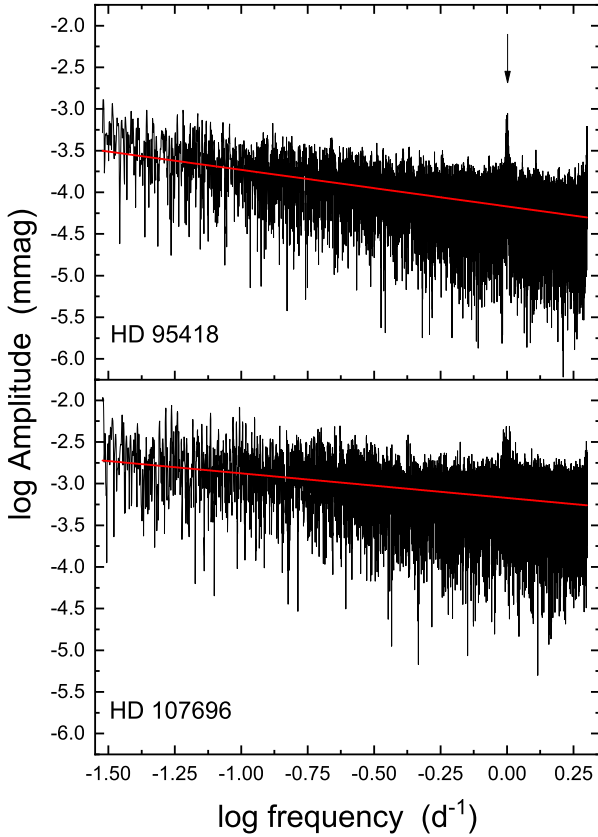


Figure 6. Logarithmic amplitude spectra of the SMEI light curves of HD 95418 (upper panel) and HD 107696 (lower panel). Also shown are the fits with the parameters listed in Table 2. In both amplitude spectra, the remains of the one-day frequency is clearly visible.

for a comparison with the observations, a much larger sample size of non-variable CP2/4 stars is needed. Although a huge amount of high-quality photometric light curves are available today, such a project – although being of great interest – is not easy to implement (Paunzen et al. 2020).

4 ASTROPHYSICAL PARAMETERS AND THE HERTZSPRUNG-RUSSELL-DIAGRAM

In this section, we describe the sources and methods used to create the Hertzsprung-Russell diagram for our target star sample.

Photometry: photometric data of the Johnson UBV and Geneva 7-colour systems were taken from the General Catalogue of Photometric data² and the All-Sky Compiled Catalogue of 2.5 million stars (ASCC, Kharchenko 2001), whereas the Strömgren-Crawford $uvby\beta$ indices were gleaned from the catalogue by Paunzen (2015).

No Johnson ($U - B$) colours are available for HD 3980, HD 18519, HD 54118, HD 59635, HD 166596, HD 168733, and HD 183806. The full set of Strömgren-Crawford $uvby\beta$ indices was

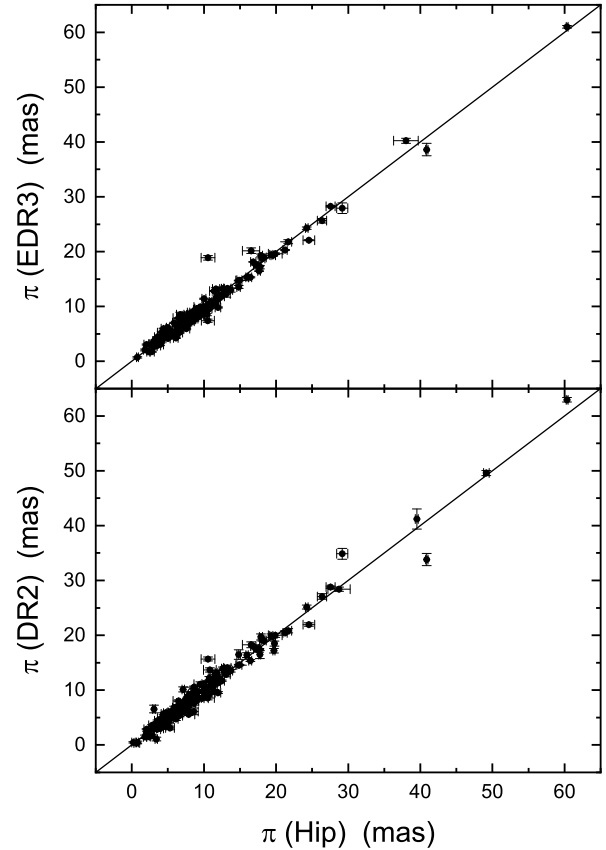


Figure 7. Comparison of the parallaxes from the *Hipparcos* catalogue to the *Gaia* EDR3 parallaxes (upper panel) and the *Gaia* DR2 parallaxes (lower panel). Several obvious outliers are visible in both plots.

measured for all objects, except for HD 4853. Geneva 7-colour photometry is not available for HD 21699, HD 23408, HD 108662, HD 108945, HD 172728, HD 177003, HD 182568, HD 185872, and HD 189178.

Reddening: as was shown by Netopil et al. (2008), the commonly employed dereddening procedures published by Napiwotzki et al. (1993) are also applicable to CP2/4 stars. They were therefore used for the reddening estimation of all objects except HD 4853, in which case we used the reddening map³ by Green et al. (2019), which is based on Gaia parallaxes and stellar photometry from Pan-STARRS 1 and 2MASS. Because this star is located in the solar vicinity (distance of 82 pc), the reddening is negligible.

For the calibrations of the different photometric systems, we used the following relations (Paunzen et al. 2006):

$$A_V = 3.1E(B - V) = 4.3E(b - y) = 4.95E(B2 - V1). \quad (2)$$

A value of 0.01 mag in $E(b - y)$ was adopted for all objects.

Bolometric correction: we used the correlation given by Netopil et al. (2008), which was tailored for the use with CP stars.

Luminosity: today, regarding bright stars, we are in the lucky position to have parallaxes available from both the *Hipparcos* (van

² <http://gcpd.physics.muni.cz/>

³ <http://argonaut.skymaps.info/>

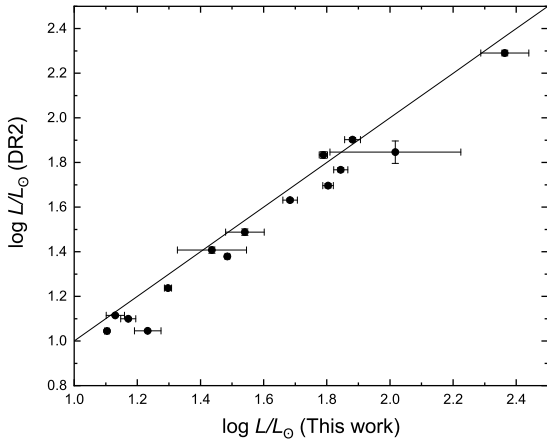


Figure 8. Comparison of the luminosities derived in this work and the *Gaia* DR2 catalogue. The latter appear systematically too low.

Leeuwen 2007) and the *Gaia* (Gaia Collaboration et al. 2018; Lindgren et al. 2018; Gaia Collaboration et al. 2020) space missions. Because our sample consists of stars between magnitudes 1.5 and 7 (Fig. 1), we checked the consistency of both data sources. Only HD 36485 has no parallax listed in the *Hipparcos* catalogue, whereas measurements for 11 stars (HD 29305, HD 35497, HD 77653, HD 81188, HD 93030, HD 96097, HD 103192, HD 116656, HD 170000, HD 196524, and HD 203585) and 16 stars (HD 29305, HD 35497, HD 40312, HD 77653, HD 81188, HD 93030, HD 96097, HD 97633, HD 103192, HD 112185, HD 116656, HD 134759, HD 170000, HD 196524, HD 202444, and HD 203585) are missing in the *Gaia* DR2 and EDR3, respectively.

In Fig. 7, we present the comparison of the parallaxes from the *Hipparcos* and *Gaia* data releases. In general, the agreement is very good, but some outliers are present. We have checked the available literature to search for reasons to account for these discrepancies. Most likely, binarity or circumstellar envelopes are at the root of the observed outlying positions, but it is out of the scope of this paper to investigate this issue in detail and to decide which of the parallax sources is the most reliable one.

Parallaxes were used in the sequence EDR3, DR2, and *Hipparcos*, depending on their availability. The parallax values were used to calculate the final luminosities listed in Table A1; a full error propagation was applied.

Gaia DR2 also includes luminosities for objects with effective temperatures less than 10 000 K (Cochetti et al. 2020). Corresponding luminosities were obtained for 15 stars from our list. A comparison of the *Gaia* DR2 luminosities to our values is provided in Figure 8, from which it is obvious that the *Gaia* DR2 luminosities are systematically too low and should be used with caution for CP2/4 stars.

Effective temperature: if available, data from the Johnson *UBV*, Geneva 7-colour, and Strömgren-Crawford *uvby* photometric systems were used. Netopil et al. (2008) introduced calibrations for CP stars using individual corrections for the temperature domain and the CP subclass, which are summarised in their Table 2. We here follow their approach. For the derivation of the final effective

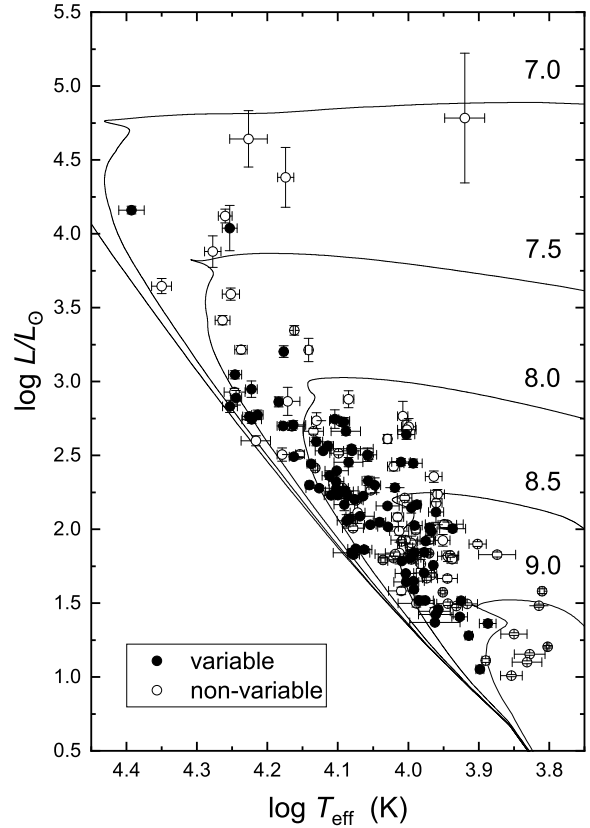


Figure 9. Positions of our target stars in the Hertzsprung-Russell diagram, which is provided in the form of $\log T_{\text{eff}}$ versus $\log L/L_{\odot}$ (Table A1). Also shown are stellar evolutionary models for the indicated logarithmic ages by Ekström et al. (2012).

temperatures, all calibrated values were averaged and the standard deviations were calculated.

Mass and Evolutionary Phase: to estimate these parameters, we employed the Stellar Isochrone Fitting Tool⁴, which builds on the methodology of Malkov et al. (2010) in estimating the mass, age, radius, and evolutionary phase of a star according to its effective temperature and luminosity. The tool automatically searches for similar data in models based on evolutionary tracks and selects the four grid points closest to the input value in the Hertzsprung-Russell diagram. From these grid points, the output parameters are obtained by repetitive linear interpolation.

The final astrophysical parameters are listed in Table A1. In Fig. 1 (lower panel), the distribution of the effective temperatures is shown. Most stars have values between 9 000 and 13 000 K, which corresponds to spectral types between A2 and B8, in agreement with the peak distribution of CP stars. As expected, there is also an extension to cooler and hotter temperatures that covers the whole range of the CP star phenomenon.

In Fig. 9, the Hertzsprung-Russell diagram is presented together with non-rotating isochrones from Ekström et al. (2012) for

⁴ <https://github.com/Johaney-s/StIFT>

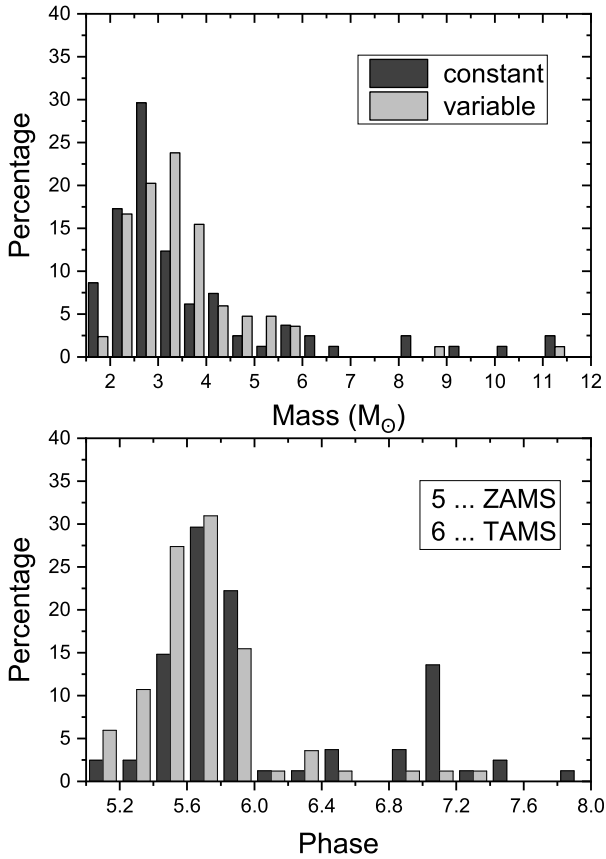


Figure 10. Histograms of the masses and evolutionary phases of the constant and variable CP2/4 stars. The coding of the evolutionary phase follows the isochrone grid of [Bressan et al. \(2012\)](#).

$[Z] = 0.014$. The choice of the metallicity rests on the analysis presented in Sect. 4.2.2. of [Hümmerich et al. \(2020\)](#). It is based on published individual abundances for stars of our target star sample. No object is located below the zero-age main sequence, but several stars are close to the terminal-age main sequence, which implies that they are past the core-hydrogen burning stage and do not belong to luminosity class V. The most significantly deviating object is HD 68601. It was classified as ApSr on the basis of S2/68 UV spectra by [Cucchiari et al. \(1978\)](#). Later on, it was classified as A5 Ib by [Gray & Garrison \(1989\)](#), which is compatible with its location in the Hertzsprung-Russell diagram as shown in Fig. 9. The Δa value, which provides a measure of peculiarity by an estimation of the 5200 Å flux depression, is slightly positive (+10 mmag, [Vogt et al. 1998](#)). Unfortunately, no detailed elemental abundance studies are available in the literature. Spectroscopic studies of this interesting and apparently evolved star are encouraged.

Figure 10 shows the mass and evolutionary status of the sample divided into variable (Table 1) and constant (Table 2) stars. The coding for the evolutionary status was taken from the isochrone grid by [Bressan et al. \(2012\)](#). The mass distribution peaks at about three solar masses, as expected from the effective temperature distribution (Figure 1). Interestingly, variable stars show significantly higher masses than constant ones. This is expected because high-mass

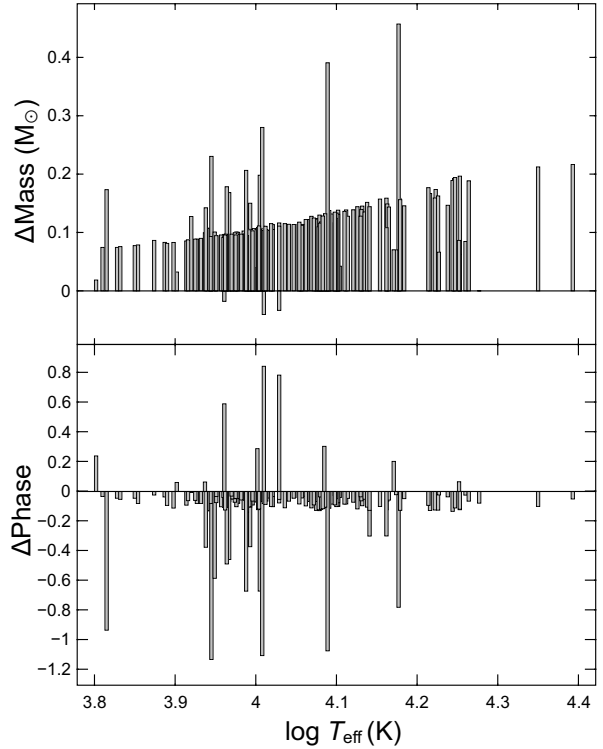


Figure 11. Differences of mass and evolutionary phase estimated from tracks with $[Z] = 0.020$ and $[Z] = 0.014$.

CP2/4 stars usually have He and Si spots, which are known to produce higher-amplitude variations than Sr, Cr, or Eu spots.

The age distribution is similar to the distributions of the fainter ACV variables investigated by [Bernhard et al. \(2015\)](#); [Hümmerich et al. \(2016\)](#); [Bernhard et al. \(2020\)](#). There is a conspicuous lack of young stars close to or at the zero-age main sequence. Almost all objects have ages between 100 Myr and 1 Gyr (Figure 9), which still places them on the main sequence but already significantly above the zero-age main sequence line. Variable stars seem to be in a more advanced evolutionary status than the constant ones. This information is important for theories dealing with the origin of the observed magnetic fields in these objects. Over the last years, a body of evidence has been built up which strongly favours the fossil field theory, which postulates that the magnetic fields are relics of the “frozen-in” interstellar magnetic field ([Braithwaite & Cantiello 2013](#)). Our results imply that spots on the stellar surface, which are thought to be coupled to the magnetic field strength, only appear after the star has spent some time on the main-sequence. From studies of open clusters ([Bagnulo et al. 2003](#); [Pöhl et al. 2003](#); [Landstreet et al. 2008](#)), it has been established that young CP2/4 stars exist, although they seem to be rare. Young CP2/4 stars are present in the large sample of stars published by [Hümmerich et al. \(2020\)](#), although they are conspicuously underrepresented. The reasons for the observed uneven distribution of CP2/4 stars are still unresolved and a matter of debate.

Finally, we checked the influence of the metallicity on the mass and evolutionary phase distribution. For this, we used an identical isochrone grid for $[Z] = 0.020$ and calibrated the target star sample as described above. In Fig. 11, the differences of mass and evo-

lutionary phase in the sense "0.020 – 0.014" is shown. Derived masses are between 0.1 and 0.2 M_{\odot} larger for the higher metallicity, which is well below 5% for the investigated mass range (Fig. 10). The evolutionary phase is constantly about 0.1 smaller in the sense that higher metallicity results in younger ages. Again, these absolute differences are negligible when compared to the observational uncertainties and possible effects such as unknown binarity. The bin size used for the analysis presented in Fig. 10 is 0.2 for the evolutionary phase. About 10% of the stars from our sample do not follow the general trend. These are the objects situated close to, or slightly above, the terminal-age main sequence. The observed sudden "jump" with the isochrone's metallicity is due to the corresponding shift in luminosity for the same effective temperature, which decides whether these objects are still calibrated as core hydrogen-burning objects or not.

5 CONCLUSIONS

Using SMEI data, we investigated the light curves of 165 CP2 and CP4 stars and candidates selected from the catalogue by [Renson & Manfroid \(2009\)](#). Because of the presence of strong instrumental trends, a basic cleaning algorithm was introduced, and instrumentally-introduced frequencies were identified and subtracted from the data sets in an automated way.

The time series analysis was performed using the Generalized Lomb-Scargle algorithm and the Phase-Dispersion Method. Because both methods complement each other and are sensitive to the different light curve characteristics and instrumental effects, this approach was found to work well with SMEI data and to derive the most reliable results.

Apart from performing thorough time-series analyses, it is also important to establish criteria defining constancy. We found that the noise of the amplitude spectra can be well described as flicker (or pink) noise, which, when plotting the logarithm of the frequency versus the logarithm of the amplitude, is characterised by a linear law that describes the mean noise level over the investigated frequency domain. Corresponding parameters for all apparently constant stars were presented.

In total, we processed and analysed 165 individual light curves from which 84 show variability in the accuracy limit of the SMEI data. We compared the derived periods with published literature values and found an excellent agreement, which proves that SMEI data are well suited to the long-term study of ACV variables.

As last step, we used calibrations specifically developed for CP stars as well as *Hipparcos* and *Gaia* data to estimate the effective temperatures and luminosities for our target star sample. Masses and evolutionary stages were calibrated using an appropriate isochrone grid. The derived astrophysical parameters provide a coherent picture of ACV variables being concentrated towards the end of their main-sequence lifetime. Our mass estimates support that He and Si peculiarities – preferentially found in the hotter, and thus more massive, CP stars – produce larger spots or spots of higher contrast.

SMEI data fill an important gap in time in the observation of bright ACV variables, for which follow-up spectroscopic and spectropolarimetric observations are comparatively easy to achieve. The here presented results are therefore important for the future analysis and, in particular, the study of the long-term behaviour of CP2/4 star light curves, and will benefit future studies of these fascinating objects.

ACKNOWLEDGEMENTS

This paper is dedicated to Leo Warzecha who died during its preparation. EP acknowledges support by the Erasmus+ programme of the European Union under grant number 2020-1-CZ01-KA203-078200. This work has also made use of data from the European Space Agency (ESA) mission *Gaia*, processed by the *Gaia* Data Processing and Analysis Consortium (DPAC) <https://www.cosmos.esa.int/web/gaia/dpac/consortium>). Funding for the DPAC has been provided by national institutions, in particular the institutions participating in the *Gaia* Multilateral Agreement. This research has made use of the SIMBAD database, operated at CDS, Strasbourg, France.

DATA AVAILABILITY

The data underlying this article will be shared on reasonable request to the corresponding author.

REFERENCES

- Abt H. A., Golson J. C., 1962, *ApJ*, **136**, 35
 Adelman S. J., 1998, *A&AS*, **132**, 93
 Adelman S. J., Pyper D. M., 1993a, in Dworetzky M. M., Castelli F., Faragiana R., eds, *Astronomical Society of the Pacific Conference Series* Vol. 44, IAU Colloq. 138: Peculiar versus Normal Phenomena in A-type and Related Stars. p. 644
 Adelman S. J., Pyper D. M., 1993b, *A&AS*, **101**, 393
 Armstrong J. T., Mozurkewich D., Hajian A. R., Johnston K. J., Thessin R. N., Peterson D. M., Hummel C. A., Gilbreath G. C., 2006, *AJ*, **131**, 2643
 Bagnulo S., Landstreet J. D., Lo Curto G., Szeifert T., Wade G. A., 2003, *A&A*, **403**, 645
 Balona L. A., Engelbrecht C. A., 1985, *MNRAS*, **214**, 559
 Bernhard K., Hümmerich S., Otero S., Paunzen E., 2015, *A&A*, **581**, A138
 Bernhard K., Hümmerich S., Paunzen E., 2020, *MNRAS*, **493**, 3293
 Braithwaite J., Cantiello M., 2013, *MNRAS*, **428**, 2789
 Bressan A., Marigo P., Girardi L., Salasnich B., Dal Cero C., Rubele S., Nanni A., 2012, *MNRAS*, **427**, 127
 Bruntt H., et al., 2009, *MNRAS*, **396**, 1189
 Cochetti Y. R., Zorec J., Cidale L. S., Arias M. L., Aidelman Y., Torres A. F., Frémat Y., Granada A., 2020, *A&A*, **634**, A18
 Cucchiario A., Macau-Hercot D., Jaschek M., Jaschek C., 1978, *A&AS*, **33**, 15
 Cumming A., Marcy G. W., Butler R. P., 1999, *ApJ*, **526**, 890
 Dukes Robert J. J., Adelman S. J., 2018, *PASP*, **130**, 044202
 Ekström S., et al., 2012, *A&A*, **537**, A146
 Eyer L., Grenon M., Falin J. L., Froeschle M., Mignard F., 1994, *Sol. Phys.*, **152**, 91
 Eyles C. J., et al., 2003, *Sol. Phys.*, **217**, 319
 Gaia Collaboration et al., 2018, *A&A*, **616**, A1
 Gaia Collaboration Brown A. G. A., Vallenari A., Prusti T., de Bruijne J. H. J., Babusiaux C., Biermann M., 2020, arXiv e-prints, [p. arXiv:2012.01533](https://arxiv.org/abs/2012.01533)
 Ghazaryan S., Alecian G., Hakobyan A. A., 2018, *MNRAS*, **480**, 2953
 Ghazaryan S., Alecian G., Hakobyan A. A., 2019, *MNRAS*, **487**, 5922
 Gray R. O., Garrison R. F., 1989, *ApJS*, **70**, 623
 Green G. M., Schlafly E., Zucker C., Speagle J. S., Finkbeiner D., 2019, *ApJ*, **887**, 93
 Hartman J. D., Bakos G. Á., 2016, *Astronomy and Computing*, **17**, 1
 Hensberge H., et al., 1981, *A&AS*, **46**, 151
 Hick P., Buffington A., Jackson B. V., 2007, in Fineschi S., Viereck R. A., eds, *Society of Photo-Optical Instrumentation Engineers (SPIE) Conference Series* Vol. 6689, *Solar Physics and Space Weather Instrumentation II*. p. 66890C, [doi:10.1117/12.734808](https://doi.org/10.1117/12.734808)

Horne J. H., Baliunas S. L., 1986, *ApJ*, **302**, 757
Hümmerich S., Paunzen E., Bernhard K., 2016, *AJ*, **152**, 104
Hümmerich S., Bernhard K., Paunzen E., Hamsch F.-J., Bohlens T., Powles J., 2017, *MNRAS*, **466**, 1399
Hümmerich S., Paunzen E., Bernhard K., 2020, *A&A*, **640**, A40
Jackson R. J., Jeffries R. D., 2013, *MNRAS*, **431**, 1883
Jagelka M., Mikulášek Z., Hümmerich S., Paunzen E., 2019, *A&A*, **622**, A199
Jerzykiewicz M., Sterken C., 1977, *Acta Astron.*, **27**, 365
Kallinger T., et al., 2017, *A&A*, **603**, A13
Kharchenko N. V., 2001, *Kinematika i Fizika Nebesnykh Tel*, **17**, 409
Landstreet J. D., et al., 2008, *A&A*, **481**, 465
Le Contel J. M., Mathias P., Chapellier E., Valtier J. C., 2001, *A&A*, **380**, 277
Lindgren L., et al., 2018, *A&A*, **616**, A2
Malkov O. Y., Sichevskij S. G., Kovaleva D. A., 2010, *MNRAS*, **401**, 695
Manfroid J., Renson P., 1994, *A&A*, **281**, 73
Manfroid J., et al., 1991, *A&AS*, **87**, 481
Mathys G., 2017, *A&A*, **601**, A14
Mathys G., Manfroid J., 1985, *A&AS*, **60**, 17
Mikulášek Z., 2016, *Contributions of the Astronomical Observatory Skalnaté Pleso*, **46**, 95
Napiwotzki R., Schoenberner D., Wenske V., 1993, *A&A*, **268**, 653
Netopil M., Paunzen E., Maitzen H. M., North P., Hubrig S., 2008, *A&A*, **491**, 545
Netopil M., Paunzen E., Hümmerich S., Bernhard K., 2017, *MNRAS*, **468**, 2745
Paunzen E., 2015, *A&A*, **580**, A23
Paunzen E., Maitzen H. M., 1998, *A&AS*, **133**, 1
Paunzen E., Vanmunster T., 2016, *Astronomische Nachrichten*, **337**, 239
Paunzen E., Stütz C., Maitzen H. M., 2005, *A&A*, **441**, 631
Paunzen E., Schnell A., Maitzen H. M., 2006, *A&A*, **458**, 293
Paunzen E., et al., 2019, *MNRAS*, **485**, 4247
Paunzen E., Janík J., Krtička J., Mikulášek Z., Zejda M., 2020, in Neiner C., Weiss W. W., Baade D., Griffin R. E., Lovekin C. C., Moffat A. F. J., eds, *Stars and their Variability Observed from Space*. pp 19–24
Peterson D. M., 1970, *ApJ*, **161**, 685
Pöhl H., Maitzen H. M., Paunzen E., 2003, *A&A*, **402**, 247
Pojmanski G., 2002, *Acta Astron.*, **52**, 397
Pollacco D. L., et al., 2006, *PASP*, **118**, 1407
Preston G. W., 1974, *ARA&A*, **12**, 257
Renson P., Manfroid J., 2009, *A&A*, **498**, 961
Ricker G. R., et al., 2015, *Journal of Astronomical Telescopes, Instruments, and Systems*, **1**, 014003
Romanyuk I. I., Kudryavtsev D. O., 2008, *Astrophysical Bulletin*, **63**, 139
Romanyuk I. I., Semenko E. A., Yakunin I. A., Kudryavtsev D. O., 2013, *Astrophysical Bulletin*, **68**, 300
Samus' N. N., Kazarovets E. V., Durlevich O. V., Kireeva N. N., Pastukhova E. N., 2017, *Astronomy Reports*, **61**, 80
Stellingwerf R. F., 1978, *ApJ*, **224**, 953
Stibbs D. W. N., 1950, *MNRAS*, **110**, 395
Subba Rao T., Priestley M. B., Lessi O., 1997, *Applications of time series analysis in astronomy and meteorology*
Tang S., Grindlay J., Los E., Servillat M., 2013, *PASP*, **125**, 857
Vogt N., Kerschbaum F., Maitzen H. M., Faundez-Abans M., 1998, *A&AS*, **130**, 455
Walczak P., et al., 2019, *MNRAS*, **485**, 3544
Watson C. L., Henden A. A., Price A., 2006, *Society for Astronomical Sciences Annual Symposium*, **25**, 47
Weiss W. W., et al., 2020, *A&A*, **642**, A64
Williams W. E., Frantz R. L., Breger M., 1974, *A&A*, **35**, 381
Winzer J. E., 1974, PhD thesis, UNIVERSITY OF TORONTO (CANADA).
Wraight K. T., Fossati L., Netopil M., Paunzen E., Rode-Paunzen M., Bewsher D., Norton A. J., White G. J., 2012, *MNRAS*, **420**, 757
Zechmeister M., Kürster M., 2009, *A&A*, **496**, 577
Ziznovsky J., 1983, *Information Bulletin on Variable Stars*, **2366**, 1
Zverko J., 1984, *Bulletin of the Astronomical Institutes of Czechoslovakia*, **35**, 294

Zverko J., Zboril M., Ziznovsky J., 1994, *A&A*, **283**, 932
Zwintz K., et al., 2019, *A&A*, **627**, A28
van Leeuwen F., 2007, *A&A*, **474**, 653

APPENDIX A: ESSENTIAL DATA FOR OUR SAMPLE STARS

Table A1 lists essential data for our sample stars. It is organised as follows:

- Column 1: HD number.
- Column 2: Identifier from Renson & Manfroid (2009).
- Column 3: Right ascension (J2000). Positional information was taken from GAIA DR2 (Gaia Collaboration et al. 2018; Lindgren et al. 2018).
- Column 4: Declination (J2000).
- Column 5: Spectral classification from Renson & Manfroid (2009).
- Column 6: Mean V magnitude.
- Column 7: Mean V magnitude error.
- Column 8: Parallax (Hipparcos).
- Column 9: Parallax error.
- Column 10: Parallax (Gaia DR2).
- Column 11: Parallax error.
- Column 12: Parallax (Gaia EDR3).
- Column 13: Parallax error.
- Column 14: Absorption in the V band.
- Column 15: Mean effective temperature.
- Column 16: Mean effective temperature error.
- Column 17: Luminosity.
- Column 18: Luminosity error.
- Column 19: Mass.
- Column 20: Evolutionary Phase.

Table A1. Essential data for our sample stars, sorted by increasing right ascension. The columns denote: (1) HD number. (2) Identifier from [Renson & Manfroid \(2009\)](#). (3) Right ascension (J2000; GAIA DR2). (4) Declination (J2000; GAIA DR2). (5) Spectral classification from [Renson & Manfroid \(2009\)](#). (6) Mean *V* magnitude. (7) Mean *V* magnitude error. (8) Parallax (Hipparcos). (9) Parallax error. (10) Parallax (Gaia DR2). (11) Parallax error. (12) Parallax (Gaia EDR3). (13) Parallax error. (14) Absorption in the *V* band. (15) Mean effective temperature. (16) Mean effective temperature error. (17) Luminosity. (18) Luminosity error. (19) Mass. (20) Evolutionary Phase.

(1)	(2)	(3)	(4)	(5)	(6)	(7)	(8)	(9)	(10)	(11)	(12)	(13)	(14)	(15)	(16)	(17)	(18)	(19)	(20)	
HD	ID _{RM09}	RA(J2000)	Dec(J2000)	Spl _{RM09}	<i>V</i> mag	<i>e_v</i> (Hip)	<i>π</i> (Hip)	<i>π</i> (DR2)	<i>π</i> (DR3)	<i>e_π</i> (DR2)	<i>e_π</i> (DR3)	<i>Δ_v</i>	<i>log L/L_⊙</i>	<i>e_{log L/L_⊙}</i>	<i>e_{log T_{eff}}</i>	<i>log L/L_⊙</i>	<i>e_{log L/L_⊙}</i>	Mass	Phase	
1280	270	00 17 05.496	+38 40 53.91	A2:Si:Sr	4.607	0.005	10.56	15.685	0.383	18.875	0.425	0.000	3.944	0.014	0.014	1.67	0.02	2.16	5.65	
2064	490	00 25 06.402	+53 02 48.36	B9:Si	5.760	0.010	7.89	5.560	0.199	8.188	0.138	0.038	4.053	0.008	0.008	2.26	0.02	3.43	3.84	
3980	1690	00 41 46.399	-50 30 00.83	A7:Si:Eu:Cr	5.698	0.003	14.92	14.033	0.090	14.770	0.041	0.000	3.914	0.005	0.005	1.28	0.01	1.91	5.37	
4953	1280	00 34 53.131	-50 42 26.00	A3:Si	5.607	0.015	11.40	12.158	0.001	12.826	0.076	0.000	3.932	0.009	0.009	1.48	0.01	2.08	5.65	
6377	1670	01 05 05.336	-14 42 46.63	B6:He:wk.	5.700	0.010	18.32	19.028	0.125	19.828	0.061	0.000	3.828	0.023	0.023	1.13	0.08	1.71	4.88	
10221	2550	01 42 20.514	-68 02 34.85	A0:Si:Cr	5.570	0.019	8.39	7.682	0.173	7.696	0.057	0.000	4.029	0.015	0.015	2.02	0.02	2.46	5.68	
11052	2030	01 53 31.814	-19 17 18.13	A1:Si:Cr:Sr	5.380	0.009	19.88	19.983	0.346	19.627	0.183	0.000	3.998	0.004	0.004	1.88	0.02	2.57	5.66	
12753	3010	01 54 22.018	-42 29 48.89	A0:He:Pr	5.088	0.005	10.63	10.483	0.247	10.185	0.139	0.000	3.998	0.004	0.004	1.88	0.02	2.67	5.73	
12767	3260	02 04 29.434	-29 17 48.47	A0:Si	4.686	0.005	8.79	9.616	0.263	9.403	0.133	0.000	4.112	0.011	0.011	2.36	0.02	3.62	5.60	
14392	3620	02 20 58.201	+60 09 05.44	A0:Si	5.550	0.010	8.31	7.899	0.109	8.528	0.168	0.000	4.069	0.020	0.020	2.09	0.01	3.01	5.45	
15089	3760	02 29 03.941	+67 24 08.46	A4:Si	4.503	0.006	24.55	21.960	0.333	22.080	0.118	0.000	3.927	0.011	0.011	2.04	0.02	2.04	5.63	
18519	4630	02 57 12.719	+21 20 25.09	A3:Ti	5.556	0.008	9.84	9.848	0.258	9.345	0.132	0.000	4.041	0.009	0.009	2.05	0.02	2.99	5.69	
18529	4630	02 59 12.719	+21 20 25.09	A3:Ti	5.556	0.008	9.84	9.848	0.258	9.345	0.132	0.000	4.041	0.009	0.009	2.05	0.02	2.99	5.69	
19400	4850	03 02 15.449	-71 54 09.04	B8:He:wk.	5.520	0.007	6.34	6.536	0.099	6.500	0.062	0.000	4.132	0.003	0.003	2.41	0.01	3.77	5.51	
19832	4910	03 32 08.596	+48 01 24.58	B8:He:wk.	5.465	0.004	5.79	6.041	0.172	7.867	0.065	0.038	4.088	0.013	0.013	2.06	0.04	3.14	5.36	
22470	5710	03 36 17.393	-17 28 01.55	B9:Si	5.222	0.004	5.39	5.912	0.151	5.638	0.154	0.146	4.178	0.009	0.009	2.70	0.02	4.52	5.59	
22470	5710	03 36 17.393	-17 28 01.55	B9:Si	5.222	0.004	5.39	5.912	0.151	5.638	0.154	0.146	4.178	0.009	0.009	2.70	0.02	4.52	5.59	
22920	5840	03 40 38.335	+24 22 03.72	B7:He:wk.	5.529	0.014	4.27	5.352	0.169	5.240	0.092	0.031	4.131	0.009	0.009	2.32	0.04	3.40	5.51	
23408	6000	03 45 49.602	-05 12 03.77	B8:Si	3.869	0.003	8.51	8.279	0.478	6.683	0.761	0.310	4.104	0.006	0.006	2.75	0.06	4.57	6.11	
23850	6100	03 49 09.744	+24 03 12.15	B8:He:wk.	3.621	0.003	8.53	8.629	0.856	8.118	0.479	0.100	4.076	0.010	0.010	2.20	0.02	3.32	5.67	
25267	6440	03 59 55.478	-24 00 58.79	A0:Si	4.645	0.015	9.96	10.665	0.211	9.974	0.100	0.000	4.102	0.010	0.010	2.27	0.02	3.44	5.54	
25823	6560	04 06 36.408	+27 35 59.51	B9:Si:Si	5.194	0.005	7.76	8.205	0.169	8.067	0.106	0.000	4.102	0.010	0.010	2.27	0.02	3.44	5.54	
25823	6560	04 06 36.408	+27 35 59.51	B9:Si:Si	5.194	0.005	7.76	8.205	0.169	8.067	0.106	0.000	4.102	0.010	0.010	2.27	0.02	3.44	5.54	
26961	6880	04 18 14.605	+50 17 43.81	A2:Si	4.592	0.003	10.40	9.558	0.763	8.547	0.234	0.000	4.075	0.011	0.011	1.92	0.02	2.85	5.10	
27309	7010	04 19 36.695	+21 46 24.68	A0:Si:Cr	5.380	0.010	10.00	11.442	0.204	11.402	0.095	0.000	4.075	0.011	0.011	1.90	0.02	2.40	7.07	
28319	7240	04 28 39.716	+15 52 15.12	A8:Si	3.988	0.004	21.69	20.835	0.373	21.813	0.374	0.114	4.098	0.012	0.012	1.87	0.02	2.40	7.07	
28843	7420	04 32 37.560	-03 12 34.39	B9:He:wk.	5.799	0.020	6.86	5.903	0.114	5.896	0.061	0.053	4.162	0.006	0.006	2.49	0.02	4.05	5.36	
29009	7480	04 33 54.733	-06 44 20.10	B9:Si	5.713	0.004	3.94	3.722	0.127	4.181	0.076	0.034	4.064	0.007	0.007	2.73	0.03	3.94	5.86	
29305	7490	04 33 59.785	-05 02 42.10	A0:Si	3.262	0.004	19.34	19.34	0.31	6.970	0.063	0.034	4.064	0.007	0.007	2.73	0.03	3.94	5.86	
30612	7940	04 43 03.948	-70 55 51.79	B9:Si	5.523	0.006	6.64	6.64	0.23	6.841	0.075	0.000	4.094	0.008	0.008	2.28	0.01	3.23	5.70	
32549	8280	05 04 34.140	+15 24 15.01	B9:Si:Cr	4.680	0.010	8.93	9.343	0.394	7.807	0.140	0.000	3.996	0.013	0.013	2.15	0.04	3.14	6.25	
32650	8350	05 12 22.433	+73 56 47.93	B9:Si	5.447	0.005	8.63	10.529	0.228	8.935	0.230	0.000	4.062	0.011	0.011	1.86	0.02	2.97	5.48	
34968	8933	05 20 26.906	-21 14 22.91	B9:He:wk.	4.703	0.005	7.84	8.719	0.166	7.822	0.112	0.000	4.005	0.010	0.010	2.21	0.02	3.08	6.56	
35039	8953	05 21 45.751	-00 22 56.87	B2:He	4.729	0.012	3.51	4.987	0.351	2.859	0.158	0.128	4.277	0.012	0.012	3.88	0.11	8.00	7.08	
35497	9110	05 26 17.514	+28 36 27.12	B8:Cr:Mn	1.650	0.008	24.36	2.573	0.077	2.625	0.054	0.135	4.246	0.009	0.009	2.73	0.01	4.17	5.90	
36485	9440	05 32 00.413	-00 17 04.19	B2:He	6.847	0.022	7.89	8.848	0.199	8.188	0.264	0.000	3.959	0.010	0.010	2.24	0.02	2.80	5.85	
38104	10240	05 45 54.039	+49 49 34.56	A1:Cr:Eu	5.461	0.010	7.69	7.143	0.176	6.855	0.096	0.000	3.991	0.011	0.011	2.02	0.02	2.65	5.85	
39317	10560	05 52 22.300	+14 10 18.45	B9:Si:Eu:Cr	5.550	0.010	19.70	17.183	0.411	17.183	0.411	0.176	6.855	0.096	0.096	0.000	4.010	0.013	2.64	6.25
40312	10780	05 59 43.245	+37 12 45.28	A0:Si	2.645	0.029	19.70	17.183	0.411	17.183	0.411	0.176	6.855	0.096	0.096	0.000	4.010	0.013	2.64	6.25
40394	10790	06 00 58.568	+47 54 06.94	A0:Si:Fe	5.732	0.024	2.82	3.588	0.127	3.155	0.082	0.185	4.003	0.012	0.012	2.64	0.03	3.86	7.23	
42509	1320	06 12 01.340	+19 47 26.00	B9:Si	5.770	0.010	3.92	3.929	0.189	3.086	0.209	0.000	4.000	0.010	0.010	2.69	0.05	3.66	7.19	
42660	1320	06 35 24.175	+36 46 47.34	B9:Si	5.770	0.010	3.92	3.929	0.189	3.086	0.209	0.000	4.000	0.010	0.010	2.69	0.05	3.66	7.19	
47152	1400	07 08 53.333	-28 38 03.81	A0:He:wk.	5.290	0.003	6.40	6.324	0.024	6.294	0.062	0.000	4.102	0.016	0.016	2.40	0.01	3.53	5.62	
47152	1400	07 08 53.333	-28 38 03.81	A0:He:wk.	5.290	0.003	6.40	6.324	0.024	6.294	0.062	0.000	4.102	0.016	0.016	2.40	0.01	3.53	5.62	
54718	1480	07 12 13.331	-50 29 58.62	A3:Si:Cr	5.151	0.003	9.84	10.483	0.182	10.363	0.163	0.000	3.945	0.020	0.020	1.94	0.02	2.61	5.72	
55718	15140	07 12 13.331	-50 29 58.62	A3:Si:Cr	5.151	0.003	9.84	10.483	0.182	10.363	0.163	0.000	3.945	0.020	0.020	1.94	0.02	2.61	5.72	
56022	15400	07 13 13.539	-45 10 37.84	A0:Si:Cr:Si	4.857	0.004	7.93	7.066	0.152	7.564	0.095	0.000	3.985	0.013	0.013	2.03	0.02	2.60	7.05	
56455	15400	07 13 13.539	-45 10 37.84	A0:Si:Cr:Si	4.857	0.004	7.93	7.066	0.152	7.564	0.095	0.000	3.985	0.013	0.013	2.03	0.02	2.60	7.05	
56455	15400	07 13 13.539	-45 10 37.84	A0:Si:Cr:Si	4.857	0.004	7.93	7.066	0.152	7.564	0.095	0.000	3.985	0.013	0.013	2.03	0.02	2.60	7.05	
56																				

Table A1. Essential data for our sample stars, sorted by increasing right ascension. The columns denote: (1) HD number. (2) Identifier from [Renson & Manfroid \(2009\)](#). (3) Right ascension (J2000; GAIA DR2). (4) Declination (J2000; GAIA DR2). (5) Spectral classification from [Renson & Manfroid \(2009\)](#). (6) Mean *V* magnitude. (7) Mean *V* magnitude error. (8) Parallax (Hipparcos). (9) Parallax error. (10) Parallax (Gaia DR2). (11) Parallax error. (12) Parallax (Gaia EDR3). (13) Parallax error. (14) Absorption in the *V* band. (15) Mean effective temperature. (16) Mean effective temperature error. (17) Luminosity. (18) Luminosity error. (19) Mass. (20) Evolutionary Phase.

(1) HD	(2) ID_RM09	(3) RA(J2000)	(4) Dec(J2000)	(5) SpT_RM09	(6) <i>V</i> mag	(7) <i>V</i> mag error	(8) π (Hip)	(9) π error (Hip)	(10) π (DR2)	(11) π error (DR2)	(12) π (EDR3)	(13) π error (EDR3)	(14) A_V	(15) $\log T_{\text{eff}}$	(16) $\log T_{\text{eff}}$ error	(17) $\log L/L_{\odot}$	(18) $\log L/L_{\odot}$ error	(19) Mass	(20) Phase	
103192	29760	11 52 24.543	-33 54 29.35	B9 Si	4.278	0.004	10.53	0.60	15.387	0.174	15.331	0.107	0.000	4.047	0.008	2.30	0.05	3.29	5.81	
106661	30870	12 16 00.181	+14 53 36.61	A2 Si	5.097	0.009	16.42	0.20	9.692	0.157	9.609	0.072	0.023	3.493	0.015	1.50	0.01	2.15	5.63	
107693	31230	12 22 49.422	-57 40 33.95	B8 Cr	5.380	0.008	9.02	0.29	12.286	0.233	11.283	0.109	0.135	3.874	0.026	1.83	0.02	2.42	7.15	
108283	31440	12 26 20.064	+27 16 05.69	A9 Si	5.910	0.002	11.82	0.24	11.286	0.233	11.283	0.109	0.135	3.874	0.026	1.83	0.02	2.42	7.15	
108426	31450	12 26 20.064	+27 16 05.69	A9 Si	5.910	0.002	11.82	0.24	11.286	0.233	11.283	0.109	0.135	3.874	0.026	1.83	0.02	2.42	7.15	
108942	31610	12 31 55.860	-21 34 01.84	B3 He, wk	5.432	0.004	12.60	0.27	11.997	0.196	12.029	0.122	0.000	3.951	0.003	1.57	0.01	2.21	5.69	
109026	31640	12 32 38.003	-72 07 58.95	B3 He, wk	3.860	0.008	10.04	0.13	9.796	0.383	8.602	0.280	0.002	4.184	0.005	2.86	0.03	5.01	5.69	
112185	32580	12 54 01.706	+55 57 34.98	B7 He, wk	1.763	0.012	39.51	0.20	41.216	1.839	11.698	0.090	0.000	3.967	0.008	1.99	0.04	2.72	5.87	
115735	33470	13 18 14.514	+49 40 55.38	B9 He, wk	5.139	0.010	11.87	0.23	13.037	0.260	13.228	0.129	0.000	4.021	0.022	1.81	0.01	2.62	5.52	
116458	33590	13 25 50.288	-70 37 38.05	A0 He, Cr	5.663	0.004	7.35	0.30	7.759	0.181	7.992	0.117	0.000	4.004	0.021	1.92	0.04	2.60	5.70	
116656	33650	13 25 56.632	+54 55 29.25	A2 Si, Si	2.053	0.009	38.01	1.71	40.213	38.01	40.213	0.462	0.000	3.951	0.010	1.52	0.01	2.47	5.50	
118022	34020	13 34 07.949	+03 39 32.43	A2 Cr, He, Si	4.929	0.011	17.65	0.20	17.162	0.229	16.944	0.122	0.068	3.976	0.011	1.52	0.01	2.47	5.50	
120198	34660	13 46 35.679	+54 25 57.63	A0 He, Cr, Si	5.685	0.021	11.23	0.23	10.619	0.069	10.742	0.042	0.000	4.003	0.018	1.64	0.01	2.21	5.41	
120640	34740	13 51 47.221	+65 53 55.14	B3 He	5.769	0.012	2.05	0.36	2.879	0.102	3.069	0.092	0.106	4.264	0.021	3.41	0.03	6.48	5.71	
120709	34750	13 51 49.605	-32 59 38.73	B5 He, wk, P	4.565	0.010	9.49	0.89	11.098	0.427	9.910	0.165	0.101	4.216	0.021	2.60	0.01	4.75	5.19	
123255	35336	14 06 42.883	+09 18 48.63	F1 Cr	5.464	0.011	17.23	0.37	17.504	0.148	17.563	0.099	0.049	4.009	0.018	1.29	0.01	1.86	5.84	
124224	35560	14 12 15.805	+02 24 33.81	B9 Si	5.011	0.011	12.63	0.21	13.937	0.260	13.228	0.129	0.000	4.078	0.008	1.83	0.02	2.89	5.12	
124252	35810	14 13 40.770	+00 50 43.49	F7 Mg, Cr, Si	4.977	0.017	16.84	0.37	18.012	0.094	18.127	0.049	0.000	3.802	0.002	1.20	0.01	1.73	6.36	
125823	35910	14 23 02.237	-59 50 42.60	B3 He, wk	4.379	0.044	7.13	0.16	10.130	0.439	8.329	0.180	0.058	4.235	0.011	2.83	0.04	5.60	5.35	
128996	36710	14 42 30.399	+54 58 30.54	A9 Si, He	3.177	0.010	40.53	0.14	62.944	0.429	60.523	0.226	0.077	3.998	0.006	2.05	0.01	1.75	5.45	
129000	36710	14 42 30.399	+54 58 30.54	A9 Si, He	3.177	0.010	40.53	0.14	62.944	0.429	60.523	0.226	0.077	3.998	0.006	2.05	0.01	1.75	5.45	
130100	37075	14 46 10.676	+54 58 30.54	A9 Si, He	3.177	0.010	40.53	0.14	62.944	0.429	60.523	0.226	0.077	3.998	0.006	2.05	0.01	1.75	5.45	
130100	37075	14 46 10.676	+54 58 30.54	A9 Si, He	3.177	0.010	40.53	0.14	62.944	0.429	60.523	0.226	0.077	3.998	0.006	2.05	0.01	1.75	5.45	
130100	37075	14 46 10.676	+54 58 30.54	A9 Si, He	3.177	0.010	40.53	0.14	62.944	0.429	60.523	0.226	0.077	3.998	0.006	2.05	0.01	1.75	5.45	
130100	37075	14 46 10.676	+54 58 30.54	A9 Si, He	3.177	0.010	40.53	0.14	62.944	0.429	60.523	0.226	0.077	3.998	0.006	2.05	0.01	1.75	5.45	
130158	37080	14 47 22.559	-25 37 27.23	B9 Si	5.611	0.008	4.39	0.34	5.882	0.174	5.982	0.074	0.002	4.086	3.974	0.006	1.67	0.01	2.40	5.67
131120	37270	14 52 51.080	-77 48 11.38	B7 He, wk	5.021	0.003	6.63	0.22	6.956	0.401	6.964	0.166	0.087	4.244	0.007	2.89	0.05	3.14	5.86	
133880	38010	15 08 12.134	+00 55 02.27	B9 Si	5.791	0.010	9.03	0.33	9.652	0.244	9.492	0.079	0.000	4.081	0.026	1.84	0.02	2.88	5.06	
134759	38230	15 12 13.285	-19 47 30.18	B9 Si	4.533	0.005	8.59	0.25	7.650	0.405	8.59	0.333	0.060	3.964	0.012	2.36	0.04	3.08	7.13	
135382	38430	15 18 54.601	+68 40 46.24	A1 He	2.877	0.008	17.74	0.12	16.496	0.174	17.181	0.112	0.112	4.072	0.011	2.11	0.07	3.13	5.54	
136933	38890	15 24 45.010	-39 42 36.79	A0 Si	5.373	0.005	8.02	0.62	8.367	0.714	8.273	0.970	0.056	3.987	0.012	1.36	0.03	2.14	5.87	
137909	39200	15 27 49.722	+29 06 20.28	A9 Si, Cr, He	3.678	0.013	29.17	0.76	34.867	0.989	27.826	0.279	0.089	4.008	0.020	2.26	0.02	3.43	5.58	
138764	39515	15 34 26.589	+09 11 00.29	B6 Si	5.166	0.009	8.17	0.58	8.729	0.227	8.489	0.145	0.094	4.098	0.020	2.26	0.02	3.43	5.58	
138769	39515	15 35 53.240	+44 57 30.06	B3 He, wk	4.538	0.004	7.62	0.43	7.311	0.466	6.846	0.132	0.686	4.132	0.004	1.46	0.01	5.32	5.60	
140160	39840	15 41 47.415	+12 50 51.19	A1 Si	5.322	0.017	14.84	0.41	14.551	0.133	14.722	0.075	0.000	3.957	0.004	1.46	0.01	2.13	5.50	
140728	39990	15 52 30.772	+52 21 39.26	A0 Si, Cr	5.510	0.010	10.92	0.18	10.896	0.081	10.894	0.250	0.000	4.004	0.015	1.70	0.01	2.47	5.47	
142990	40340	15 53 20.057	-20 10 01.21	B3 He, wk	5.031	0.006	10.34	0.91	8.365	0.317	7.388	0.290	0.461	4.214	0.008	1.77	0.01	5.06	5.55	
142990	40340	15 53 20.057	-20 10 01.21	B3 He, wk	5.031	0.006	10.34	0.91	8.365	0.317	7.388	0.290	0.461	4.214	0.008	1.77	0.01	5.06	5.55	
142990	40340	15 53 20.057	-20 10 01.21	B3 He, wk	5.031	0.006	10.34	0.91	8.365	0.317	7.388	0.290	0.461	4.214	0.008	1.77	0.01	5.06	5.55	
142990	40340	15 53 20.057	-20 10 01.21	B3 He, wk	5.031	0.006	10.34	0.91	8.365	0.317	7.388	0.290	0.461	4.214	0.008	1.77	0.01	5.06	5.55	
142990	40340	15 53 20.057	-20 10 01.21	B3 He, wk	5.031	0.006	10.34	0.91	8.365	0.317	7.388	0.290	0.461	4.214	0.008	1.77	0.01	5.06	5.55	
148112	41810	16 05 14.654	+41 01 59.77	B0 He, wk	4.570	0.010	13.04	0.64	13.515	0.338	13.105	0.166	0.000	4.226	0.009	2.76	0.01	4.90	5.16	
148112	41810	16 05 14.654	+41 01 59.77	B0 He, wk	4.570	0.010	13.04	0.64	13.515	0.338	13.105	0.166	0.000	4.226	0.009	2.76	0.01	4.90	5.16	
148330	41910	16 24 35.334	+55 12 18.28	A2 Si, Si	5.740	0.010	8.34	0.22	8.038	0.052	8.151	0.188	0.044	3.971	0.002	1.84	0.01	2.53	5.77	
148330	41910	16 24 35.334	+55 12 18.28	A2 Si, Si	5.740	0.010	8.34	0.22	8.038	0.052	8.151	0.188	0.044	3.971	0.002	1.84	0.01	2.53	5.77	
148330	41910	16 24 35.334	+55 12 18.28	A2 Si, Si	5.740	0.010	8.34	0.22	8.038	0.052	8.151	0.188	0.044	3.971	0.002	1.84	0.01	2.53	5.77	
148330	41910	16 24 35.334	+55 12 18.28	A2 Si, Si	5.740	0.010	8.34	0.22	8.038	0.052	8.151	0.188	0.044	3.971	0.002	1.84	0.01	2.53	5.77	
148330	41910	16 24 35.334	+55 12 18.28	A2 Si, Si	5.740	0.010	8.34	0.22	8.038	0.052	8.151	0.188	0.044	3.971	0.002	1.84	0.01	2.53	5.77	
148330	41910	16 24 35.334	+55 12 18.28	A2 Si, Si	5.740	0.010	8.34	0.22	8.038	0.052	8.151	0.188	0.044	3.971	0.002	1.84	0.01	2.53	5.77	
148330	41910	16 24 35.334	+55 12 18.28	A2 Si, Si	5.740	0.010	8.34	0.22	8.038	0.052	8.151	0.188	0.044	3.971	0.002	1.84	0.01	2.53	5.77	
148330	41910	16 24 35.334	+55 12 18.28	A2 Si, Si	5.740	0.010	8.34	0.22	8.038	0.052	8.151	0.188	0.044	3.971	0.002	1.84	0.01	2.53	5.77	
148330	41910	16 24 35.334	+55 12 18.28	A2 Si, Si	5.740	0.010	8.34	0.22	8.038	0.052	8.151	0.188	0.044	3.971	0.002	1.84	0.01	2.53	5.77	
148330	41910	16 24 35.334	+55 12 18.28	A2 Si, Si	5.740	0.010	8.34	0.22	8.038	0.052	8.151	0.188	0.044	3.971	0.002	1.84	0.01	2.53	5.77	
148330	41910	16 24 35.334	+55 12 18.28	A2 Si, Si	5.740	0.010	8.34	0.22	8.038	0.052	8.151	0.188	0.044	3.971	0.002	1.84	0.01	2.53	5.77	
148330	41910	16 24 35.334	+55 12 18.28	A2 Si, Si	5.740	0.010	8.34	0.22	8.038	0.052	8.1									